Determining the onset of hydrodynamic erosion in turbulent flow

J. C. Salevan,[1] Abram H. Clark,[2,1] Mark D. Shattuck,[3,1]
Corey S. O'Hern,[1,4,5] and Nicholas T. Ouellette[6]

[1]*Department of Mechanical Engineering and Materials Science, Yale University,
New Haven, Connecticut 06520, USA*
[2]*Department of Physics, Naval Postgraduate School, Monterey, California 93943, USA*
[3]*Benjamin Levich Institute and Physics Department, The City College of the City University of New York,
New York, New York 10031, USA*
[4]*Department of Physics, Yale University, New Haven, Connecticut 06520, USA*
[5]*Department of Applied Physics, Yale University, New Haven, Connecticut 06520, USA*
[6]*Department of Civil and Environmental Engineering, Stanford University, Stanford, California 94305, USA*

We revisit the longstanding question of the onset of sediment transport driven by a turbulent fluid flow via laboratory measurements. We use particle-tracking velocimetry to quantify the fluid flow as well as the motion of individual grains. As we increase the flow speed above the threshold for sediment transport, we observe that an increasing fraction of grains is transported downstream, although the average downstream velocity of the transported grains remains roughly constant. However, we find that the fraction of mobilized grains does not vanish sharply at a critical flow rate. Additionally, the distribution of the fluctuating velocities of nontransported grains becomes broader with heavier tails, meaning that unambiguously separating mobile and static grains is not possible. As an alternative approach, we quantify the statistics of grain velocities by using a mixture model consisting of two forms for the grain velocities: a decaying-exponential tail, which represents grains transported downstream, and a peaked distribution centered at zero velocity, which represents grains that fluctuate due to the turbulent flow but remain in place. Our results suggest that more sophisticated statistical measures may be required to quantify grain motion near the onset of sediment transport, particularly in the presence of turbulence.

I. INTRODUCTION

The transport of sediment by flowing water is a fundamental physical process with broad applications in fields ranging from geomorphology to land use and agriculture [1–3]. In many of these applications, the source of sediment is a bed of granular or other erodible material over which the water flows. If the stress delivered to the bed by the water is too weak, the bed will not be mobilized and it will be stable; but once the stress becomes large enough, the bed will become unstable and sediment will be entrained into the flow. Thus, understanding the conditions under which bed grains first start to move, often called incipient motion [4], is of immense practical importance. Incipient motion is typically considered to be determined by the Shields number Θ [5], which compares the shear stress τ exerted by the fluid on the bed to the buoyancy-reduced gravitational stress $(\rho_g - \rho_f)gd$, where ρ_g and ρ_f are the mass densities of the grains and fluid, respectively, g is the gravitational acceleration, and d is the diameter of a typical grain. The threshold for incipient motion is often quantified by measuring the sediment flux q [6,7] as a function of Θ and identifying a critical value Θ_c above which grain velocities are nonzero.

However, this simple picture is incomplete for a variety of reasons. Both fluid forces [8,9] and grain dynamics [10,11] change qualitatively with the strength of the fluid driving, as quantified by the shear Reynolds number Re_* at the grain scale, meaning that there may not be a single sharp transition to incipient motion [12]. Previous studies have observed granular creep as the bed begins to

mobilize [13], suggesting a nonsharp transition, but also long transients [14,15], suggesting an underlying bifurcation of some kind. Moreover, incipient motion is inherently stochastic due to disorder and variation in the bed structure [16], and turbulent fluctuations from the fluid begin to play a role at moderate to high Reynolds number [17–20]. The presence of these fluctuations suggests that one may need to consider not only the mean stress but also the impulses imparted to grains via turbulent fluctuations [21,22]. Thus, describing incipient grain motion involves mapping out the evolution of grain motion in a high-dimensional parameter space and therefore is an ongoing scientific challenge.

Here, based on the results of laboratory experiments in which we measured grain trajectories near incipient motion in a turbulent flow, we argue that since incipient motion is a stochastic process, it is best captured by a careful characterization of its statistics. We used high-speed imaging and particle-tracking velocimetry to measure both the fluid flow and the grain motion. We quantify grain motion via the probability density function $P(u_g)$ of streamwise grain velocities u_g. We find that $P(u_g)$ is well described by a mixture model that is the sum of a function that is peaked at $u_g = 0$ (which we fit to a Student's t distribution), corresponding to grains that are not transported downstream but still fluctuate in place due to the turbulent flow, and a function with an exponential tail for positive u_g, corresponding to transported grains. We find that as Θ is increased above the threshold for incipient motion, the increase in sediment flux arises almost exclusively from an increased number of transported grains, while the average downstream velocity of mobile grains remains constant. Additionally, we find that the velocity distribution of nontransported grains becomes broader near the incipient motion threshold and thus the sediment flux does not vanish sharply.

We begin below in Sec. II by describing our experimental methods, including the flow apparatus, the bed preparation protocols, and the measurement techniques. In Sec. III we describe our results in the context of previous studies. Section III A describes selected prior approaches used to characterize incipient motion along with similar measurements from our data and Sec. III B describes our approach where we fit grain velocity statistics to a mixture model. Finally, in Sec. IV we summarize and contextualize our results.

II. EXPERIMENT

A. Apparatus

Our experimental apparatus is a closed racetrack-shaped channel consisting of two straight sections joined by two U-shaped curves, as shown in Fig. 1. The channel width is a uniform 5.08 cm and its height is 21.25 cm. We drive the fluid flow with a toothed H series timing belt connected to a external rotary motor. The trapezoidal belt teeth span the width of the belt (3.8 cm), which is slightly smaller than the width of the channel (5.08 cm). The center-to-center spacing between the belt teeth is 1.27 cm. The base width (in the streamwise direction) of the trapezoidal tooth is 6.12 mm and the width of the top of the tooth is 4.45 mm. The teeth protrude by 2.29 mm. The belt is fully immersed in water and is mounted to the top of one of the straight sections. The fluid velocity is controlled via the voltage sent to the motor controller. To calibrate the fluid driving, we measure the fluid velocity in the test section directly (described in Sec. II B) and correlate that measurement with the voltage we apply to the motor controller. The entire apparatus is fully enclosed, so that there is no free surface. The sidewalls of the test section are made of tempered glass and the top surface of the test section is made of clear acrylic, allowing optical access for imaging.

To prepare our experiments, we first add soda lime glass beads with diameter $d = 0.1125 \pm 0.0125$ cm and density $\rho_g = 2.5$ g/cm^3 to the test section, up to a fill height of roughly 5.7 cm (about 51 grain diameters). This erodible bed is constrained in the streamwise direction by triangular wedges, which both help to slow the formation of large-scale bedforms as the experiments proceed and keep most of the grains in the test section. After the grains are added, we completely fill the apparatus with water. We then drive the fluid at a slow speed (far below the threshold for grain motion) to dispel trapped air bubbles in the system. We note that this weak fluid forcing also allows
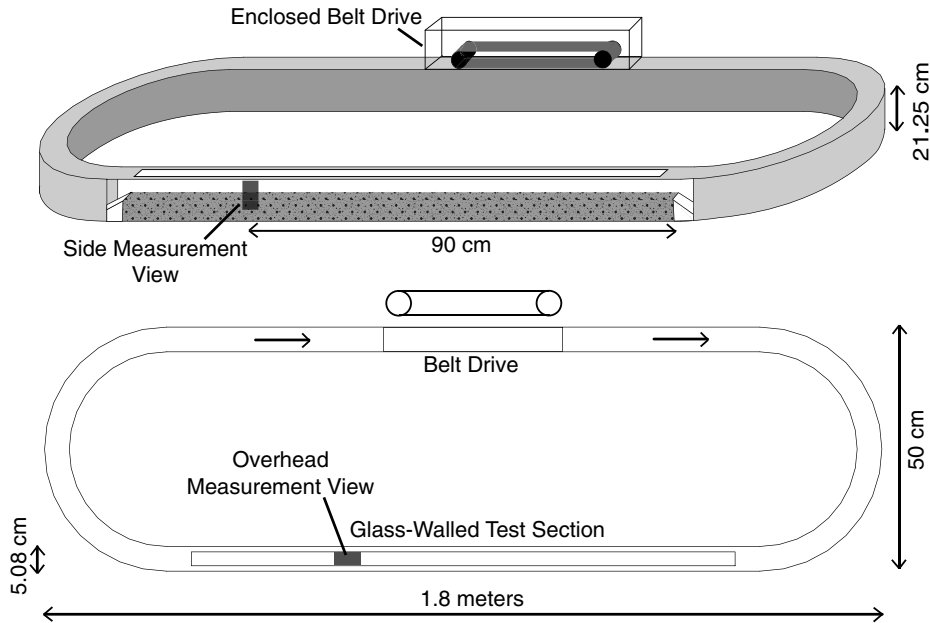
FIG. 1. Schematic of the experimental apparatus. The top panel shows a three-dimensional view, including the clear-walled test section with the grains and triangular wedges, and the enclosed, motorized belt drive on the opposite side. The bottom panel shows an overhead view, indicating the clockwise fluid flow direction. Overall, the apparatus is 1.8 m long, 21.25 cm tall, and 50 cm wide, with a 5.08 cm channel width. In the 1.2 m test section, the grain bed height is approximately 5.7 cm, and measurements are taken approximately 90 cm from the wedge at the entrance.

the beads on the surface of the bed to slightly rearrange. However, the grains do not move sufficiently for any bed armoring or size segregation to take place [15,23].

To collect data on grain motion and fluid flow, we record video in a small region in the test section (shown in Fig. 1). We choose this region to be sufficiently far (that is, more than the entrance length) from the triangular wedge at the entry point of the test section that the flow is developed. Thus, we do not investigate differences in grain motion at, for example, the entry point of the test section compared with the middle of the test section.

After the initial state is prepared, we quasistatically increase the freestream fluid velocity in increments of approximately 0.95 cm/s up to a maximum velocity for a given experimental run. After each increment, we allow the flow to stabilize and then acquire data. We reset the initial bed state as described above before each set of experiments. The granular bed and the fluid flow are imaged separately: One camera views the bed from overhead, through the top of the test section, to image the bed surface, and a second camera views the fluid flow through a side window, to image the velocity profile of the fluid flow.

B. Fluid flow and shear stress

To quantify the fluid flow, we add fluorescent red polyethylene microspheres that are 75–90 μm in diameter and density matched with water. We illuminate a vertical slice in the center of the test section with a light sheet produced by a 532-nm laser and a cylindrical lens mounted above the apparatus. Particles in the light sheet fluoresce and are imaged using a high-speed camera at a frame rate of 1400 frames/s (fps) and a spatial resolution of 181 pixels/cm. We record 5-s videos through the side of the test section and track the tracer particles via a multiframe predictive particle-tracking
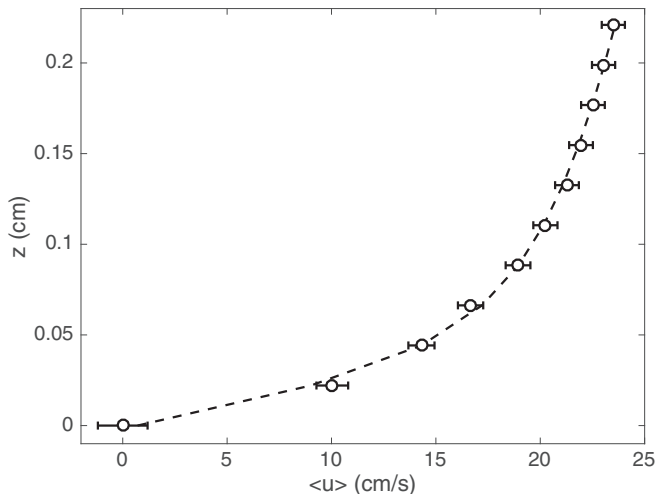
FIG. 2. Typical fluid velocity profile, as measured from the streamwise velocities u of tracer particles in the fluid. Each data point (open circles) represents a time average over all tracer particle trajectories for binned values of the height. The error bars show the standard deviation of the velocities in each bin. The dashed line is a fit following the procedure described by Rodríguez-López *et al.* [26], from which we extract the wall shear stress τ_{wall} (see the text).

algorithm [24]. Accurate velocities are then computed from the particle trajectories via convolution with a smoothing and differentiating kernel [25].

To extract the hydrodynamic stress exerted on the granular bed, we first construct the mean vertical velocity profile by binning the measured velocities in height (with at least 20 000 samples per bin). An archetypal profile is shown in Fig. 2, where the error bars show the standard deviation of the velocities in each bin. To compute the wall shear stress τ_{wall}, we fit the velocity profile using the modified logarithmic law method described by Rodríguez-López *et al.* [26], the result of which is shown as the dashed curve in Fig. 2. The wall shear stress is then given as $\tau_{\text{wall}} = \mu \frac{\partial u}{\partial y}$ evaluated at $y = 0$, where μ is the dynamic viscosity of water. The wall shear stress τ_{wall} in turn allows us to compute the friction Reynolds number $\text{Re}_\tau = \delta/\delta_\nu$, where δ is the channel half-height, $\delta_\nu = \nu\sqrt{\rho_f/\tau_{\text{wall}}}$ is the viscous length scale [27], and $\nu = \mu/\rho_f$ is the kinetic viscosity of water. For the results presented here, $450 < \text{Re}_\tau < 2200$.

The wall shear stress also allows us to compute the Shields number Θ as

$$\Theta = \frac{\tau_{\text{wall}}}{(\rho_g - \rho_f)gd}, \tag{1}$$

where in our experiments the Shields numbers are in the range $0.005 < \Theta < 0.045$. The shear Reynolds number at the grain scale $\text{Re}_* = d/\delta_\nu$ is also used to specify the sediment-transport regime, and in our experiments, we have $6 < \text{Re}_* < 30$.

C. Granular bed

To quantify the motion of bed grains, about 5% of the glass beads in the bed are colored black, which appear dark against the bright background of illuminated clear beads. Aside from the color, the black beads are identical to the clear beads. We illuminate the measurement region (see the gray rectangle in Fig. 1) with an array of light-emitting diodes and use a second camera positioned above the bed to take videos of the bed surface at 250 or 500 fps with a resolution of 190 pixels/cm. Initial data were taken at 500 fps, but we determined that 250 fps is also sufficiently fast such that beads move no more than half of a grain diameter per frame over the range of driving flows we consider.
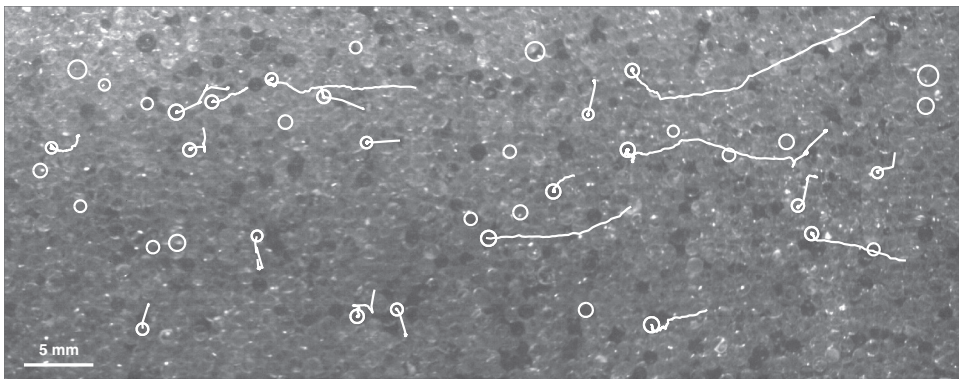
FIG. 3. Raw image of the granular bed shown from above. The physical dimensions are 6.8 cm in the horizontal streamwise direction by 2.7 cm in the vertical cross-stream direction, spanning roughly the middle half of the channel width. Selected grain trajectories are overlaid in white. This snapshot shows white circles to indicate the position and radius of a selected subset of tracked grains during a single frame, with trailing lines behind each grain indicating the motion from the beginning of each track. The time interval for each track varies, as the time at which the Lagrangian particle-tracking algorithm began to track each specific grain also varies. We include a 5-mm scale bar on the bottom left and the fluid flows from right to left.

The image shown in Fig. 3 has physical dimensions of 6.8 cm long by 2.7 cm wide. Thus, our images capturing grain motion span roughly the middle half of the channel, which is 5.08 cm wide, neglecting the areas near the outer wall. We do not investigate the dependence of grain motion in the lateral direction of the bed. However, since the flow is turbulent, we expect the fluid velocity to have only a very weak dependence on the lateral position, except perhaps at the wall where grain-wall friction becomes important.

After normalizing each image to correct for lighting inhomogeneities, we use a circular Hough transform to locate the position of black beads on the bed surface accurately. With those positions, we then use the same Lagrangian particle-tracking algorithm as used for the fluid flow to extract trajectories for each bead. Figure 3 shows an archetypal raw image frame from a video of the granular bed. Selected grain trajectories are shown in white, with the current position of each grain in the frame shown as a white circle, indicating both the position and the radius extracted from the Hough transform. We note that when we allow the experiment to run for very long times, we observe propagating bedforms (e.g., ripples). However, we reset the bed before each set of experiments, which prevents these bedforms from influencing the data we show here.

III. RESULTS

A. Comparison with selected previous approaches

Incipient motion is typically defined as the point at which the sediment flux q vanishes. If all grain motion is associated with downstream transport, then the mean grain velocity $\langle u_g \rangle$ should be proportional to q; thus, since $\langle u_g \rangle$ is typically easier to measure, it is often used as a proxy for q in determining the onset of sediment transport. In Fig. 4(a) we plot $\langle u_g \rangle$ as a function of Θ, where in our case the average is taken over all measured velocities for each tracked grain. For small Θ, $\langle u_g \rangle$ is approximately zero. For $\Theta > 0.023$, we observe that $\langle u_g \rangle$ clearly grows, but the exact value of Θ where this growth begins is unclear. In addition to the mean grain velocity, we can also investigate the standard deviation of grain velocity σ_g, since we would expect variation among the grains and in time. Figure 4(b) shows σ_g for the grain velocity as a function of Θ. Although it varies in a qualitatively similar way as $\langle u_g \rangle$ with Θ, σ_g does not vanish for small Θ; instead, the magnitude of
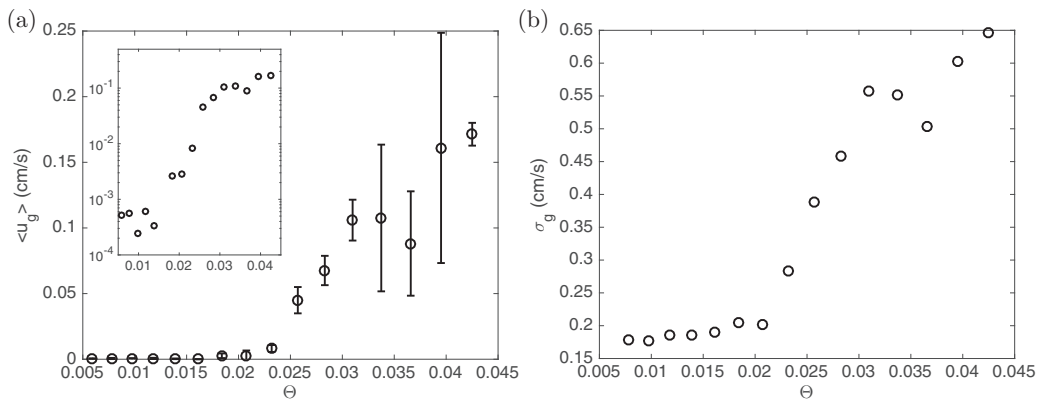
FIG. 4. (a) Mean grain velocity $\langle u_g \rangle$ as a function of Shields number Θ. The error bars show the standard error computed for six trials and the inset shows the same data plotted on semilogarithmic axes. (b) Standard deviation of grain velocity σ_g as a function of Θ.

the fluctuations in grain velocity remain finite. This result suggests that even below the onset of net sediment transport, grains can rattle on the surface of the bed.

Measuring the mean grain velocity is not the only method that has been used to determine the onset of sediment transport. For example, several recent studies [7,28,29] have taken the approach of first choosing a velocity threshold to identify which grains are in motion. The ratio of the number of these "active" grains to the total number of grains or the bed surface area is known as the particle or grain activity. The critical Shields number Θ_c can ideally be determined by identifying the point at which the grain activity vanishes [7]. After identifying mobilized grains, one can examine the statistics of the velocities of moving grains, since the grain flux q is proportional to the product of the grain activity and the mean velocity. The probability density function (PDF) $P_m(u_g)$ of the velocities u_g of mobile grains is often found to be close to exponential [7,28,30,31], so it is well fit by

$$P_m(u_g) = \frac{1}{u_g^*} e^{-u_g/u_g^*}. \tag{2}$$

Here u_g^* is the average velocity of the mobile grains. This distribution can be derived from maximum-entropy statistical-mechanical arguments, starting from a microcanonical ensemble and constraining the total grain momentum [30]. Equation (2) is particularly successful for describing bedload transport when the number of moving grains becomes large [30,31]. However, this entire approach is predicated on first identifying moving grains. Nevertheless, very close to the threshold of incipient motion, the grain activity and subsequent velocity statistics may become highly sensitive to the choice of threshold, especially when the driving flow is turbulent. In this case, the transition to sustained sediment transport may not be sharp, but may be blurred by the turbulent fluctuations in the driving flow.

Figure 5(a) shows activity distributions from our experiments. Each curve shows a PDF of the fraction of active grains n_{active} in any given video frame from all experiments at a given value of Θ, where active grains are defined as those that have an instantaneous streamwise velocity greater than a threshold velocity $u_{\text{threshold}}$. These PDFs are sensitive to the choice of $u_{\text{threshold}}$. We plot the mean fraction of active grains $\langle n_{\text{active}} \rangle$ as a function of Θ in Fig. 5(b). The behavior is qualitatively similar to the mean velocity shown in Fig. 4(a), but $\langle n_{\text{active}} \rangle$ remains nonzero in general for small Θ. The value of this plateau at small Θ is dependent on $u_{\text{threshold}}$.
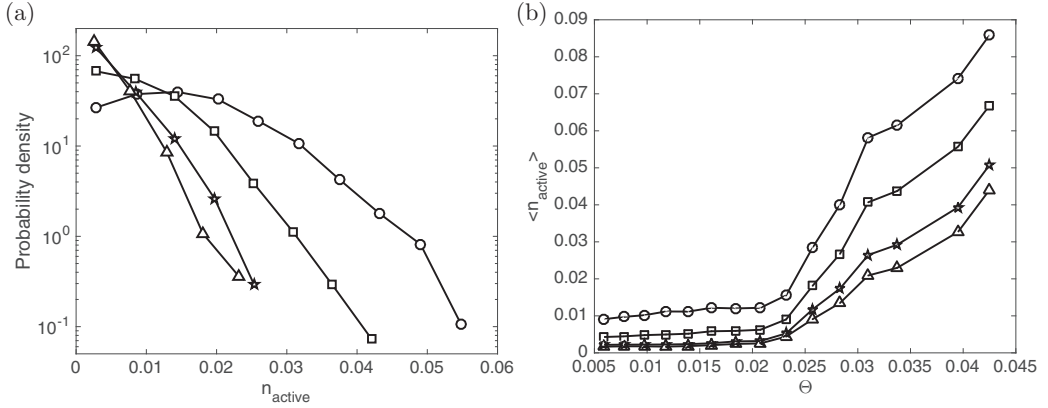
FIG. 5. (a) Probability density that a fraction n_{active} of all tracked grains is moving at any given time for $\Theta = 0.023$, plotted for four different values of the velocity threshold $u_{threshold}$ defining grain motion: 0.75 cm/s (circles), 1 cm/s (squares), 1.5 cm/s (stars), and 2 cm/s (triangles). These PDFs are highly sensitive to the choice of threshold. (b) Mean fraction of active grains for the same values of $u_{threshold}$ as a function of Θ.

B. Fitting to a mixture model

It is not surprising that mobile and nonmobile grains are difficult to separate, especially very near the onset of sustained sediment transport. This blurring arises from physical effects, primarily turbulence, as well as from finite experimental measurement accuracy. Thus, instead of identifying only mobile grains and examining their statistics, we examine *all* tracked grains together. In Fig. 6 we show PDFs of all tracked grain velocities for several values of Θ. The solid lines show measured data and the dashed lines are a model that is fit to the data, as described below. Several features of these PDFs are noteworthy. As one might expect, most of the measured particle velocities are clustered near zero. These points are from bed particles that we identify but that are not mobile, since near incipient motion most of the bed is still not moving. However, the peak at $u_g = 0$ is not sharp
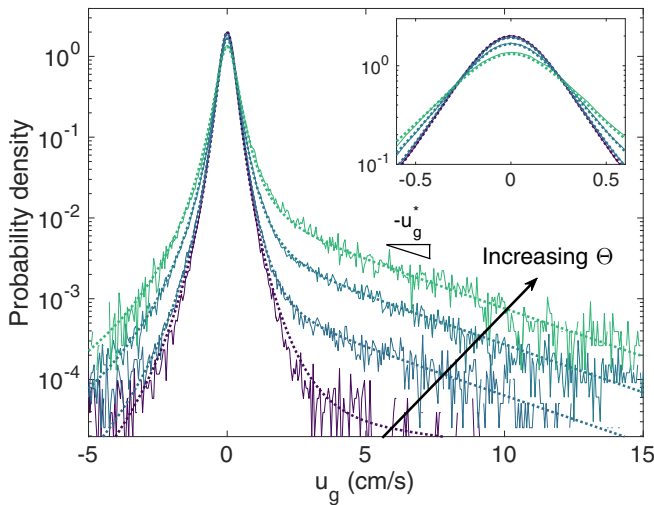

FIG. 6. The PDFs $P(u_g)$ of grain velocities u_g (solid curves), for $\Theta = 0.0059, 0.0232, 0.0283,$ and 0.0425. Dashed curves show fits of the data to Eq. (3). The inset shows a close-up of the same data near the core of the PDF.

but rather is somewhat broad, even in the low-Θ limit, which arises from a combination of physical fluctuations and experimental noise. At larger values of u_g, the PDF becomes a decaying exponential with a characteristic velocity scale u_g^*, as in Eq. (2). This part of the PDF arises from mobilized grains. Between the static and mobile parts of the PDF, there is a crossover region that does not fit well either with an exponential or with a normal distribution centered at $u_g = 0$. In addition, the magnitude of $P(u_g)$ for small velocities increases with Θ for both positive and negative u_g. Visual inspection of the crossover region for $u_g > 0$ suggests that $u_\text{threshold}$ should be chosen between 1 and 4 cm/s, but there is no objective way to choose within this range. Moreover, the width of the crossover region appears to grow with Θ, meaning that the appropriate choice for $u_\text{threshold}$ would vary with Θ.

These PDFs clearly show why activity and mean velocity are difficult to use as precise indicators of the onset of net sediment transport: The development of the exponential tail that characterizes downstream flux is gradual and occurs at the same time as the central peak broadens due to turbulence and noise. As an alternative way to quantify our data over the full range of Θ, we instead here suggest a fit of the *entire* PDF via a mixture model. As we have already indicated, the tail at positive u_g ought to be exponential. The central core due to turbulence is quasi-Gaussian; we, however, find better agreement (and are better able to fit the entire PDF) if we use a Student's t distribution instead. Thus, we fit the grain velocity PDFs to a function of the form

$$P(u_g) = A \frac{\Gamma\left(\frac{\zeta+1}{2}\right)}{\sigma\sqrt{\zeta\pi}\Gamma\left(\frac{\zeta}{2}\right)} \left[\frac{\zeta + \left(\frac{u_g}{\sigma}\right)^2}{\zeta}\right]^{[-(\zeta+1)/2]} + B\frac{1}{u_g^*}e^{-u_g/u_g^*}. \tag{3}$$

Here A and B are mixture fractions that sum to unity (to keep the overall PDF normalized) and give the relative fraction of particles in the (static) core and the (mobile) tail; Γ is the Gamma function; σ is the characteristic width of the t distribution and ζ is its shape parameter that sets the heaviness of its tails. When ζ is small, the tails are heavier than a Gaussian with the same variance, and as $\zeta \to \infty$, the t distribution becomes a Gaussian with standard deviation σ.

Figure 7 shows the parameters σ, ζ, u_g^*, and B that characterize Eq. (3) as a function of Θ. Although we allow both A and B to vary in our fits, we always recover $A + B = 1 \pm 0.04$. Figure 7(a) shows the characteristic width σ of the t distribution. For small Θ, σ fluctuates somewhat but remains roughly constant. For $\Theta > 0.023$, σ grows strongly. We note that we observe identical behavior for σ when we fit the core to a normal distribution, where σ is simply the standard deviation. Additionally, as shown in Fig. 7(b), we observe a decrease in ζ for $\Theta > 0.023$, meaning that the tails of the distribution are becoming heavier for both positive and negative u_g. We interpret this effect as a manifestation of the increasing turbulence (since in our experiment the Shields and Reynolds numbers vary together): The more intense turbulence implies stronger fluctuations in wall shear stress and velocity, which in turn lead to more rapid fluctuations of nonmobilized bed grains. We note that the t distribution is symmetric about zero, so the agreement of our model with the data suggests that the turbulence-driven fluctuations of the grains have similar positive and negative downstream values. By definition, the grains described by the t distribution do not contribute to the net transported flux.

For larger grain velocities, we find excellent agreement with a decaying exponential, as in Eqs. (2) and (3). Figure 7(c) shows u_g^*, which can be interpreted as the mean velocity of the transported grains. For $\Theta \geqslant 0.023$, u_g^* remains roughly constant at $u_g^* \approx 3.5$ cm/s. Thus, just above the onset of net sediment transport, increases in the grain flux appear to be primarily driven not by increasing the velocity of mobilized grains but by increasing their number. This conclusion is supported by Fig. 7(d), which shows that B, which can be roughly interpreted as the fraction of grains that fall into the exponential tail, clearly grows with increasing Θ for $\Theta > 0.023$. However, B does not vanish sharply at a particular value of Θ. This behavior can be more clearly seen in the inset of Fig. 7(d), which follows the same trend of $\langle u_g \rangle$, shown in Fig. 4(a). For $\Theta < 0.018$, B vanishes to within our experimental precision. Over roughly $0.018 < \Theta < 0.023$, we observe a transition between $B \approx 0$ for $\Theta < 0.018$ and clear growth with increasing Θ for $\Theta > 0.023$, but the precise boundaries are not
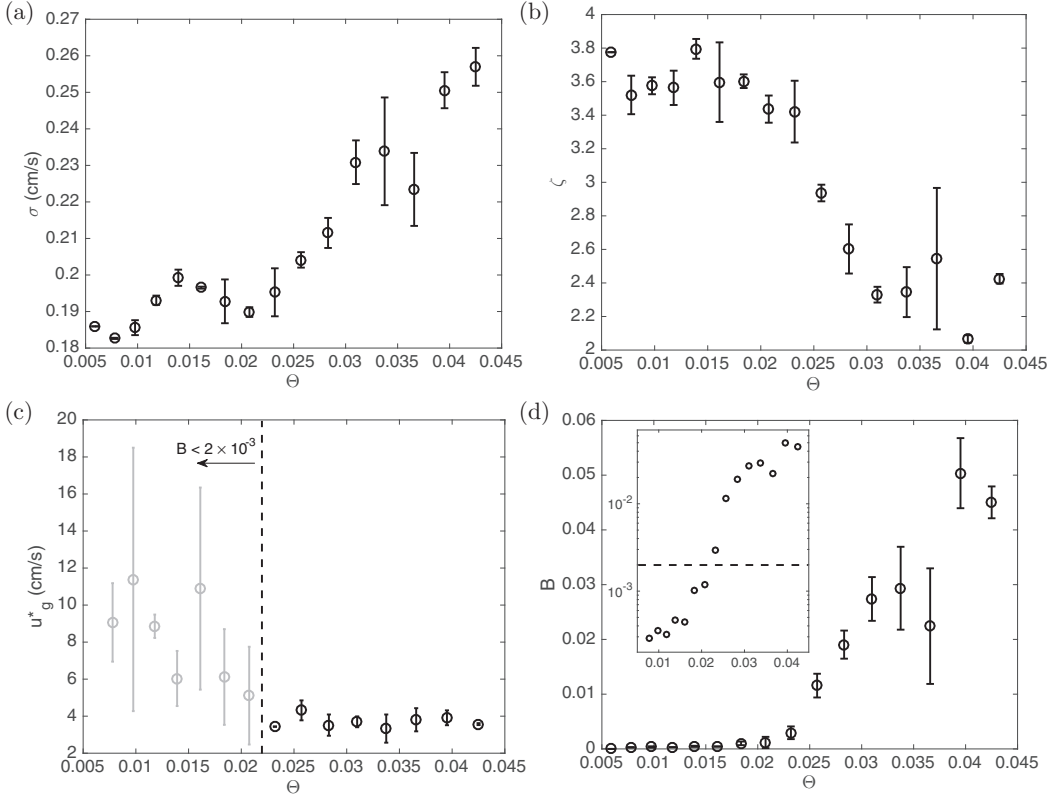
FIG. 7. Fit parameters (a) σ, (b) ζ, (c) u_g^*, and (d) B from Eq. (3) as a function of Shields number Θ. In all cases, the error bars are the standard error computed over six different experimental trials. We mark in (c) points (in gray) at which $B < 2 \times 10^{-3}$, where our fit for u_g^* is no longer physically meaningful. The inset to (d) shows the same data plotted on semilogarithmic axes, with a horizontal line at $B = 2 \times 10^{-3}$.

well defined. Thus, the transition to net sediment transport is blurred, presumably by the turbulence in our experiment.

The numerical values for B in Fig. 7(d) are similar to the values of $\langle n_{\text{active}} \rangle$ plotted in Fig. 5(b). However, fitting to Eq. (3) allows us to separate transported grains from fluctuating grains, as B vanishes for small Θ, while the fraction of active grains does not. Note that as B vanishes, our fit for u_g^* is no longer physically meaningful, as there are no transported grains. Thus, although we include data for u_g^* for all Θ, we note in Fig. 7(c) points at which $B < 2 \times 10^{-3}$. Additionally, we note that the mean velocity of mobile grains u_g^* is not the same quantity as $\langle u_g \rangle$ plotted in Fig. 4, where the latter includes all nonmoving grains that we track. Instead, one should expect $\langle u_g \rangle$ to be quantitatively similar to the product of B, the fraction of mobile grains, and u_g^*, the mean velocity of mobile grains. A comparison of $\langle u_g \rangle$ in Fig. 4(a) and B and u_g^* in Figs. 7(c) and 7(d) demonstrates that this is true.

Finally, we note that weaker grain motion at two of the six data sets at $\Theta \approx 0.037$ cause an anomalous dip in our data (Figs. 4 and 7), possibly due to a change in bed morphology during these experiments (although nothing was observable from our overhead movies). This value of Θ is significantly above onset, so we believe it does not influence our conclusions. Note that we have omitted this data point from the grain activity plots in Fig. 5. Additionally, Fig. 7 shows that u_g^* shows no change, while B and σ both decrease for this value of Θ. This is consistent with our other results, in that smaller grain flux is associated with fewer grains moving and not a decrease in the velocity of mobile grains.

IV. DISCUSSION AND CONCLUSION

Here we have presented experimental measurements of the statistics of grain motion across the transition to net sediment transport in a laboratory flow. We quantified the grain motion and the fluid flow using high-speed video and particle tracking. We considered several methods for identifying the onset of sediment transport and argued that fitting a mixture model to the full PDF of grain velocities gives the most objective way of accomplishing this goal, particularly in the presence of turbulence. Appealingly, this method does not require the choice of a threshold for deciding which grains are contributing to net sediment transport and which are simply rattling in the presence of turbulent fluctuations. Instead, the different statistical properties of these two classes of grains are used directly to distinguish them.

Using this approach, we showed that the density of grains transported downstream does not vanish sharply at a well-defined critical Shields number Θ_c. Instead, we found a crossover region somewhere below $\Theta \approx 0.023$ (roughly in the range $0.018 < \Theta < 0.023$), which is similar to Θ_c as measured in Ref. [7]. Thus, our results indicate that there may not always be a clear separation between mobile and static grains. In the PDFs of grain velocities, we found a crossover region between transported grains and immobile grains that changes as Θ is varied. Here we attribute this "blurring" of the transition to sediment transport as an effect of the turbulent fluctuations. We note, however, that this kind of continuous rather than sharp transition was also recently reported in the laminar case and interpreted as resulting from granular creep [13]. We also found that as Θ is increased above the onset of net downstream grain motion, the fraction of grains that are mobilized increases, although the mean velocity of mobilized grains remains roughly constant. This result is consistent with the findings in Ref. [28], but different from those in Ref. [7], where both activity and mean velocity of mobile grains apparently increased with increasing Θ, albeit at higher transport rates. Further work is therefore required to settle this question and to understand whether there are additional physical effects that distinguish these situations.

---

[1] W. G. Knisel, Creams: A field-scale model for chemicals, runoff and erosion from agricultural management systems, USDA Conservation Research Report No. 26, 1980 (unpublished).

[2] K. G. Renard, G. R. Foster, G. A. Weesies, D. K. McCool, and D. C. Yoder, *Predicting Soil Erosion by Water: A Guide to Conservation Planning with the Revised Universal Soil Loss Equation (RUSLE)* (United States Department of Agriculture, Washington, DC, 1997), Vol. 703.

[3] D. J Jerolmack and C. Paola, Shredding of environmental signals by sediment transport, Geophys. Res. Lett. **37**, L19401 (2010).

[4] J. M. Buffington and D. R. Montgomery, A systematic analysis of eight decades of incipient motion studies, with special reference to gravel-bedded rivers, Water Resour. Res. **33**, 1993 (1997).

[5] A. Shields, Mitteilungen der Preußischen Versuchsanstalt für Wasserbau und Schiffbau Report No. 26, 1936 (unpublished).

[6] M. Ouriemi, P. Aussillous, M. Medale, Y. Peysson, and E. Guazzelli, Determination of the critical shields number for particle erosion in laminar flow, Phys. Fluids **19**, 061706 (2007).

[7] E. Lajeunesse, L. Malverti, and F. Charru, Bed load transport in turbulent flow at the grain scale: Experiments and modeling, J. Geophys. Res. Earth Surf. **115**, F04001 (2010).

[8] P. L. Wiberg and J. D. Smith, Calculations of the critical shear stress for motion of uniform and heterogeneous sediments, Water Resour. Res. **23**, 1471 (1987).

[9] A. Kudrolli, D. Scheff, and B. Allen, Critical shear rate and torque stability condition for a particle resting on a surface in a fluid flow, J. Fluid Mech. **808**, 397 (2016).

[10] A. H. Clark, M. D. Shattuck, N. T. Ouellette, and C. S. O'Hern, Onset and cessation of motion in hydrodynamically sheared granular beds, Phys. Rev. E **92**, 042202 (2015).

[11] A. H. Clark, M. D. Shattuck, N. T. Ouellette, and C. S. O'Hern, Role of grain dynamics in determining the onset of sediment transport, Phys. Rev. Fluids **2**, 034305 (2017).

[12] D. Paphitis, Sediment movement under unidirectional flows: An assessment of empirical threshold curves, Coast. Eng. **43**, 227 (2001).

[13] M. Houssais, C. P. Ortiz, D. J. Durian, and D. J. Jerolmack, Onset of sediment transport is a continuous transition driven by fluid shear and granular creep, Nat. Commun. **6**, 6527 (2015).

[14] A. E. Lobkovsky, A. V. Orpe, R. Molloy, A. Kudrolli, and D. H. Rothman, Erosion of a granular bed driven by laminar fluid flow, J. Fluid Mech. **605**, 47 (2008).

[15] A. Hong, M. Tao, and A. Kudrolli, Onset of erosion of a granular bed in a channel driven by fluid flow, Phys. Fluids **27**, 013301 (2015).

[16] J. W. Kirchner, W. E. Dietrich, F. Iseya, and H. Ikeda, The variability of critical shear stress, friction angle, and grain protrusion in water-worked sediments, Sedimentology **37**, 647 (1990).

[17] A. D. Heathershaw and P. D. Thorne, Sea-bed noises reveal role of turbulent bursting phenomenon in sediment transport by tidal currents, Nature (London) **316**, 339 (1985).

[18] I. Nezu, H. Nakagawa, and G. H. Jirka, Turbulence in open-channel flows, J. Hydraul. Eng. **120**, 1235 (1994).

[19] O. Durán, B. Andreotti, and P. Claudin, Numerical simulation of turbulent sediment transport, from bed load to saltation, Phys. Fluids **24**, 103306 (2012).

[20] M. S. Yalin, *River Mechanics* (Elsevier, Amsterdam, 2015).

[21] P. Diplas, C. L. Dancey, A. O. Celik, M. Valyrakis, K. Greer, and T. Akar, The role of impulse on the initiation of particle movement under turbulent flow conditions, Science **322**, 717 (2008).

[22] H. Lee, M. Y. Ha, and S. Balachandar, Work-based criterion for particle motion and implication for turbulent bed-load transport, Phys. Fluids **24**, 116604 (2012).

[23] F. Charru, H. Mouilleron, and O. Eiff, Erosion and deposition of particles on a bed sheared by a viscous flow, J. Fluid Mech. **519**, 55 (2004).

[24] N. T. Ouellette, H. Xu, and E. Bodenschatz, A quantitative study of three-dimensional Lagrangian particle tracking algorithms, Exp. Fluids **40**, 301 (2006).

[25] N. Mordant, A. M. Crawford, and E. Bodenschatz, Experimental Lagrangian probability density function measurement, Physica D **193**, 245 (2004).

[26] E. Rodríguez-López, P. J. K. Bruce, and O. R. H. Buxton, A robust post-processing method to determine skin friction in turbulent boundary layers from the velocity profile, Exp. Fluids **56**, 6 (2015).

[27] S. B. Pope, *Turbulent Flows* (Cambridge University Press, Cambridge, 2000).

[28] J. C. Roseberry, M. W. Schmeeckle, and D. J. Furbish, A probabilistic description of the bed load sediment flux: 2. Particle activity and motions, J. Geophys. Res. Earth Surf. **117**, F03032 (2012).

[29] C. González, D. H. Richter, D. Bolster, S. Bateman, J. Calantoni, and C. Escauriaza, Characterization of bedload intermittency near the threshold of motion using a Lagrangian sediment transport model, Environ. Fluid Mech. **17**, 111 (2017).

[30] D. J. Furbish and M. W. Schmeeckle, A probabilistic derivation of the exponential-like distribution of bed load particle velocities, Water Resour. Res. **49**, 1537 (2013).

[31] S. L. Fathel, D. J. Furbish, and M. W. Schmeeckle, Experimental evidence of statistical ensemble behavior in bed load sediment transport, J. Geophys. Res. Earth Surf. **120**, 2298 (2015).